Site C0012[1]

M. Strasser, B. Dugan, K. Kanagawa, G.F. Moore, S. Toczko, L. Maeda, Y. Kido, K.T. Moe, Y. Sanada, L. Esteban, O. Fabbri, J. Geersen, S. Hammerschmidt, H. Hayashi, K. Heirman, A. Hüpers, M.J. Jurado Rodriguez, K. Kameo, T. Kanamatsu, H. Kitajima, H. Masuda, K. Milliken, R. Mishra, I. Motoyama, K. Olcott, K. Oohashi, K.T. Pickering, S.G. Ramirez, H. Rashid, D. Sawyer, A. Schleicher, Y. Shan, R. Skarbek, I. Song, T. Takeshita, T. Toki, J. Tudge, S. Webb, D.J. Wilson, H.-Y. Wu, and A. Yamaguchi[2]

Chapter contents

[1] Strasser, M., Dugan, B., Kanagawa, K., Moore, G.F., Toczko, S., Maeda, L., Kido, Y., Moe, K.T., Sanada, Y., Esteban, L., Fabbri, O., Geersen, J., Hammerschmidt, S., Hayashi, H., Heirman, K., Hüpers, A., Jurado Rodriguez, M.J., Kameo, K., Kanamatsu, T., Kitajima, H., Masuda, H., Milliken, K., Mishra, R., Motoyama, I., Olcott, K., Oohashi, K., Pickering, K.T., Ramirez, S.G., Rashid, H., Sawyer, D., Schleicher, A., Shan, Y., Skarbek, R., Song, I., Takeshita, T., Toki, T., Tudge, J., Webb, S., Wilson, D.J., Wu, H.-Y., and Yamaguchi, A., 2014. Site C0012. *In* ', *Proc. IODP,* 338: Yokohama (Integrated Ocean Drilling Program). doi:10.2204/iodp.proc.338.104.2014
[2] **Expedition 338 Scientists' addresses.**

Background and objectives

Integrated Ocean Drilling Program (IODP) Expeditions 322 and 333 were designed to characterize the sedimentary and upper igneous basement inputs to the Nankai Trough subduction zone (Expedition 333 Scientists, 2012a; Underwood et al., 2010). IODP Site C0012 is located in the Shikoku Basin on the crest of a prominent basement high (Kashinosaki Knoll) on the subducting Philippine Sea plate (Figs. **F1, F2**). This location provides access to the uppermost igneous crust with modest penetration below the seafloor. The rotary core barrel (RCB) was used during Expedition 322 to collect samples to 576 meters below seafloor (mbsf), which included sampling sediment and basement (Underwood et al., 2010). During Expedition 333, the hydraulic piston coring system (HPCS), the extended punch coring system (EPCS), the extended shoe coring system (ESCS), and the RCB were used to sample sediment and igneous basement to 630.5 mbsf (Expedition 333 Scientists, 2012a). As part of its contingency operations, IODP Expedition 338 used logging while drilling (LWD)/measurement while drilling (MWD) to collect geophysical logs to 710 mbsf. Together, these drilling operations provided core and logging data through the entire sedimentary succession and into the uppermost igneous basement.

Previous coring during Expeditions 322 and 333 revealed that the sedimentary succession at Site C0012 is dominated by silty clay or silty claystone with minor lithologies, including ash, volcaniclastic sandstone, and tuff (Expedition 333 Scientists, 2012a; Underwood et al., 2010). The base of the sedimentary section is reddish-brown pelagic claystone that is older than 18.9 Ma. Interstitial water in sediment above the igneous basement shows distinct trends that are indicative of diffusive processes, chemical reactions, and interaction with chemical species in the basement. Chlorinity values start at seawater values at the seafloor but increase to >600 mM near the top of basement. This increase is influenced by hydration reactions in the sediment and diffusional exchange with basement fluid. This chlorinity profile is in contrast to the profile at IODP Site C0011, where chlorinity decreases with depth. Therefore, it is interpreted that Site C0012 is less affected by the focused flow of fluids that originate beneath the trench wedge and frontal accretionary prism. The sulfate-reduction zone at Site C0012 is at ~250 mbsf, deeper than at other sites along the Nankai margin. Shear strength is relatively low in the

doi:10.2204/iodp.proc.338.104.2014

upper 100 mbsf, which correlates to nearly constant high porosity. Below this depth, shear strength increases and porosity decreases. Porosity reaches a minimum just above the basement. Approximately 100 m of the igneous basement has been sampled and is divided into Units I (pillow lavas) and II (sheet flows with pillow lava interlayers) (Expedition 333 Scientists, 2012a). Alteration of Unit I pillow lava compositions is indicative of a reducing, low-temperature environment. Alteration of Unit II suggests oxidizing and reducing conditions, which most likely occurred at different times. Characterization of the sediment and igneous basement provide insights into the composition and origin of Kashinosaki Knoll.

The specific questions motivating the study of input Sites C0011 and C0012 include

- Is fluid circulation in basement and permeable sedimentary layers influencing heat flow and diagenesis?
- How does silica diagenesis affect physical properties at Sites C0011 and C0012?
- Was magmatic activity heterogeneous in composition and age on the backarc basin basement high (Kashinosaki Knoll)?
- How does heterogeneous alteration of oceanic crust influence geochemical and fluid budgets at the inputs in the subduction zone?
- Which factor(s) control(s) the décollement's position near the toe of the Nankai accretionary prism and the location of ramps and flats and mechanical behavior throughout?
- Does the plate boundary fault, near its updip limit of seismicity, shift position from a sediment/sediment interface (stable sliding) to a sediment/basalt interface (stick-slip)? If so, what are the causes?

To address these objectives, LWD activities in Hole C0012H were conducted as contingency operations during Expedition 338 in order to provide a full suite of petrophysical logs that can be combined with analysis of cores and seismic data for a comprehensive characterization of the subduction zone inputs. LWD data generated high-resolution sampling of sediment and 180 m of the upper basement characteristics (i.e., extending basement penetration by ~80 m), including resistivity, resistivity images, natural gamma radiation, and compressional wave velocity. Specific objectives are to understand how compressional velocity relates to compaction state and fluid sources, how chemical profiles relate to physical and chemical properties, how the structures of the sedimentary section relate to the slumping, and how structures in igneous basement relate to the alteration state. Ultimately, these analyses will help define the fluid and chemical budgets of the subduction inputs, which are important to the understanding of fluid in the accretionary prism and the subducted materials.

Operations

Site C0012

Hole C0012H

The D/V *Chikyu* arrived at Site C0012 at 1045 h on 2 December 2012; the remotely operated vehicle (ROV) was prepared with four transponders and dove at 1230 h. The ROV dropped the transponders by 2100 h, after which it was recovered to the surface and the vessel moved to the planned Hole C0012H well center by 2200 h. Dynamic positioning calibration was completed by 2345 h, and the LWD assembly, including the sonicVISION tool, was made up for running into the hole. The LWD bottom-hole assembly (BHA) began running into the hole at 0430 h on 3 December. After passing a series of mid-water tests, the LWD tools reached the seafloor when the real-time data signal was lost. After spending some time on troubleshooting operations, the tool was pulled out of the hole to the rig floor for examination and possible replacement, reaching the deck at 0245 h on 4 December. Although a jamming alert from the TeleScope was received and visual inspection found no issues with the tool, a spare TeleScope was swapped into the BHA and run back at 0645 h on 4 December. A series of tests were again run as the BHA was lowered down to the seafloor, and once all had been completed successfully, the LWD BHA was ready to spud in. Using the LWD tools to determine the mudline, the seafloor was set at 3538 m drilling depth below rig floor (DRF) (3509.5 meters below sea level), and drilling ahead resumed at 1730 h. The Schlumberger logging engineers were concerned that the sonicVISION configuration should be changed by downlink because in their estimation the real-time sonic velocity was not reliable. After close consultations with the Co-Chief Scientists, it was decided to leave the sonicVISION configuration as is and continue drilling from 3686 m DRF at 2315 h on 4 December. At 0430 h on 6 December, the planned total depth (TD) of 4238 m DRF (700 mbsf) was reached, after which an additional 10 m was drilled ahead to allow the sonicVISION tool to record an interval where resistivity was seen to increase. The final TD in Hole C0012H of 4248 m DRF (710 mbsf) was reached at 0515 h. Inclination and azimuth surveys took place during circulation, and then a spot of kill mud was set before pulling out of the hole to 1994 m DRF began, ending at 1145 h. The BHA

reached the surface at 2300 h, after which the tools were laid down and preparation for coring at Site C0002 began. Transponders were released from the seafloor and all were recovered by the watch-boat *Hakuryu Maru* by 1500 h on 7 December. The vessel then began to move to Site C0002.

Logging while drilling

Hole C0012H was drilled on the Kashinosaki Knoll in the Shikoku Basin with LWD and MWD technology (see the **"Methods"** chapter [Strasser et al., 2014a]). MWD downhole drilling parameters and LWD gamma ray, azimuthal resistivity, resistivity images, and sonic velocity data were collected from 0 to 710.0 mbsf (3538.0–4248.0 m DRF). A summary of logging tools and data collected are listed in (Table **T1**). The analysis of LWD and MWD data (Figs. **F3, F4**) clearly distinguishes basement rock from the Shikoku Basin sediment at 530.3 mbsf. Overall, eight logging units were defined: six within the sediment section and two in the basement.

Data quality

The overall quality of the logging data was determined to be fair. Because of no rotation during wash down and a rate of penetration exceeding 40 m/h, no quality resistivity images were recorded above 58.5 mbsf (3596.5 m DRF). Sharp horizontal lines, artifacts from ship heave and pipe vibration, were observed throughout the processed resistivity images. Missing data due to high stick-slip (>300 cycles/min) were also observed, with a greater concentration in the upper section (0 to ~220 mbsf) and image quality generally increasing toward the sediment/basement interface. Overall, 19.4% of the images were deemed poor quality.

Continuous, good quality compressional sonic velocities were acquired throughout the drilled interval. Through the sediment section (0.0–530.30 mbsf), shear sonic velocity data were not available because it is not possible to extract shear-wave velocities slower than the compressional velocity of the drilling mud velocity when measured by a monopole transmitter. However, shear-wave sonic velocity data were obtained in two faster intervals: 573.9–603.6 mbsf (4111.9–4141.6 m DRF) and 655.4–686.8 mbsf (4193.4–4224.8 m DRF). Quality checks on the data indicate good performance of the sonicVISION tool and good quality of the measurements.

Log characterization and interpretation

Hole C0012H logging units were characterized from visual inspection of the gamma ray, ring resistivity, and sonic velocity logs (Fig. **F4**). Eight primary logging units were identified from deviations in gamma ray values with respect to a baseline, changes in trend, and changes in overall log character. The logging units were further divided into subunits based on subtle variations in resistivity and sonic velocity (Table **T2**; Fig. **F4**). Preliminary lithologic interpretations were made based on log character and relative values, with guidance from coring at Site C0012 during Expeditions 322 and 333 (Expedition 322 Scientists, 2010c; Expedition 333 Scientists, 2012c). Prominent changes in overall log character and baseline shifts occur at 530.30 mbsf, where gamma ray values drop to <20 gAPI, resistivity increases from ~3 to >10 Ωm, and sonic velocity increases from ~1800 to >3000 m/s. This boundary is interpreted as the sediment/basement interface, which was cored during Expedition 322 in Hole C0012A and during Expedition 333 in Holes C0012E, C0012F, and C0012G at 537.81, 525.81, 520.46, and 529.69 mbsf, respectively. These cores showed that the lowermost Shikoku Basin sediment overlies basaltic oceanic basement rock, composed of both pillow basalts and sheet flows (Expedition 333 Scientists, 2012c). Given such a contrast in log parameters/character between the sediment and basement (Fig. **F5**), the sediment section (0–530.30 mbsf) and basement (530.30–710.00 mbsf) are described and interpreted separately.

Shikoku Basin sediment (0–530.30 mbsf)

Six logging units were defined within the sediment section of Hole C0012H (Figs. **F4, F6;** Table **T2**). To determine the variation in gamma ray values, a baseline of 95 gAPI was chosen because it reflects the background gamma ray value and is consistent with the baseline defined at Site C0011 in the hemipelagic, silty claystone sediment (Expedition 322 Scientists, 2010b). Lithologic interpretations of logs follow the methodology used at Site C0011 (Expedition 322 Scientists, 2010b). Below this gamma ray baseline value more sand-rich sediment is interpreted, and above this value more clay-rich sediment is interpreted. Volcanic ash and sand horizons were interpreted based on a differentiation between high and low resistivity corresponding to low gamma ray spikes: low gamma ray values with low resistivity were classified as sand and low gamma ray values with high resistivity were classified as volcanic ash. Units and subunits were chosen based on changes in abundance of interpreted sand and ash horizons.

Logging Unit I (0–144.3 mbsf)

Logging Unit I is characterized by a gradually increasing trend in gamma ray values from ~65 to 95

gAPI with minor fluctuations (Fig. F6). Resistivity is low and roughly constant (~0.7 Ωm), with a few minor increases and decreases that correspond to low gamma ray peaks. Overall, sonic *P*-wave velocity exhibits a gradual increase from ~1530 to 1650 m/s. Low gamma ray values and low resistivity exhibited through logging Unit I are interpreted to reflect sandy mud lithologies, which is supported by the low sonic velocity that is close to the velocity of seawater (1500 m/s), indicative of poorly consolidated, porous sediment (Rider, 2002).

Logging Unit II (144.3–188.1 mbsf)

The logging Unit I/II boundary was placed at 144.3 mbsf, which corresponds to a change in the character of the gamma ray and resistivity logs. Also, the sonic log shows an increase from ~1650 to 1750 m/s across this logging unit boundary. An increase in frequency and thickness of low gamma ray spikes and corresponding resistivity spikes in logging Unit II is interpreted to represent a heterogeneous mixture of sand and ash beds. The most prominent layer occurs between 147.8 and 151.9 mbsf, where gamma ray values drop to <38 gAPI and resistivity increases gradually to 1.16 Ωm before a sharp drop back to a low resistivity of ~0.9 Ωm. This 4 m thick interval is interpreted as volcaniclastic sand based on low gamma ray values and high resistivity. The base of logging Unit II (188.1 mbsf) is placed below the last interpreted ash horizon, where there is a small, stepped increase in resistivity (~1.0 Ωm) and gamma ray values reach a constant baseline.

Logging Unit III (188.1–339.6 mbsf)

At 188.1 mbsf, gamma ray values reach ~95 gAPI and remain fairly constant throughout logging Unit III with only minor fluctuations. These minor fluctuations around the constant background value of 95 gAPI are interpreted to be varying silt versus clay content alternations within the dominant hemipelagic mud. Resistivity and sonic *P*-wave velocity exhibit overall low variability and constant values (~0.9 Ωm and ~1700 m/s, respectively) throughout this unit. Within logging Unit III, occasional occurrences of thin (1–2 m) low gamma ray spikes (~80 gAPI) correspond to high-resistivity spikes (>1.2 Ωm), interpreted to be thin ash layers in a dominantly hemipelagic lithology.

Logging Unit IV (339.6–403.3 mbsf)

From 339.6 mbsf, there is an increase in abundance of thin gamma ray and resistivity spikes, with the first major downhole occurrence defining the logging Unit III/IV boundary. Unit IV was divided into two subunits based on changes in gamma ray log character. Subunit IVA (339.6–372.1 mbsf) is characterized by an overall increasing gamma ray trend above the 95 gAPI baseline and repeating thin gamma ray and resistivity spikes, suggesting an increase in the number of ash and sand beds. The last downhole occurrence of sand layers in this section marks the base of Subunit IVA (372.1 mbsf). Subunit IVB (372.1–403.3 mbsf) is characterized by overall high gamma ray values (~115 gAPI) with minor fluctuations and one interpreted thin ash layer at ~380 mbsf with low gamma ray values of 79 gAPI and a high resistivity of 2.5 Ωm. With the exception of this interpreted ash layer, resistivity remains fairly uniform in character and constant in value (~1 Ωm). Through Subunit IVB, sonic velocity exhibits an overall increase from ~1780 to 1900 m/s (Fig. F6). The character of the sonic velocity log is more variable than observed in the overlying units (Fig. F5), and the higher values may indicate a more consolidated sediment. The base of logging Unit IV is placed at 403.3 mbsf, where a step down in gamma ray values, resistivity, and sonic velocity occurs (to ~95 gAPI, ~0.8 Ωm, and ~1790 m/s, respectively).

Logging Unit V (403.3–463.5 mbsf)

The overall variation of the log data is more pronounced in logging Unit V compared to the above units (Fig. F5), especially in sonic velocity (Fig. F6). Unit V is interpreted to be a heterogeneous mixture of hemipelagic mudstone, sand, and ash. Throughout this interval, sonic velocity fluctuates between ~1800 and 2000 m/s. The top of logging Unit V is at 403.3 mbsf, where gamma ray values are ~95 gAPI. Gamma ray values exhibit an overall gradual increase to ~99 gAPI at 445.3 mbsf, with occasional low spikes (<75 gAPI) coincident with high-resistivity spikes (>1.2 Ωm). Resistivity is variable and fluctuates around 0.9 Ωm to 421.5 mbsf, where it gradually increases to ~1.3 Ωm at 426.5 mbsf before decreasing back to ~0.7 Ωm at 430.9 mbsf. From 445.3 to 450.0 mbsf, gamma ray values drop (~70 gAPI) whereas resistivity stays fairly constant at ~0.75–0.85 Ωm to the very base of the gamma ray value low at 450.0 mbsf, where there is a prominent resistivity spike (>3.0 Ωm). From 450.0 mbsf to the base of the unit (463.5 mbsf), there are no more distinguishable sand or ash horizons and gamma ray values increase from ~95 to ~105 gAPI. Resistivity exhibits a gradual decrease (from ~1.0 to 0.85 Ωm), and sonic velocity decreases from a unit high (~2100 m/s) at 452.0 mbsf to ~1900 m/s. The base of Unit V is placed at the base of this sonic velocity decrease, where gamma ray values start to drop back below the 95 gAPI baseline (Fig. F6).

Logging Unit VI (463.5–530.3 mbsf)

Logging Unit VI is the lowermost unit in the sediment section of Hole C0012H and is divided into three subunits. In the upper part of Subunit VIA, from 463.5 to 467.94 mbsf, gamma ray values exhibit a gradual decrease (from ~95 to ~60 gAPI), whereas resistivity and sonic velocity are fairly constant (~0.85 Ωm and ~2000 m/s, respectively). The base of the low gamma ray values at 467.94 mbsf corresponds to a thin (<1 m) resistivity spike (0.96 Ωm) indicating a probable ash layer. Below 467.94 mbsf, resistivity is roughly constant, with only minor fluctuations around 0.9 Ωm, and sonic velocity fluctuates between ~1900 and 2000 m/s. Gamma ray values increase to ~85 gAPI at ~483.95 mbsf. Between 483.95 and 520.4 mbsf, gamma ray values fluctuate from ~75 to 85 gAPI and resistivity is roughly constant at ~0.8 Ωm, whereas sonic velocity exhibits an overall decrease from ~2000 to ~1730 m/s. Because gamma ray values between 463.5 and 520.4 mbsf are lower than the baseline of 95 gAPI and sonic velocity is ~2000 m/s, this subunit (VIA) is interpreted as a more consolidated, sandier lithology than the overlying units (Fig. **F5**). Subunit VIB is defined from 520.4 to 526.7 mbsf because through this section, gamma ray values are constant at ~95 gAPI, resistivity gradually increases to ~1–1.15 Ωm, and velocity gradually decreases to 1740 m/s (Fig. **F6**). Subunit VIC (526.7–530.3 mbsf) is characterized by decreasing gamma ray values (to <90 gAPI), gradually increasing resistivity (to ~1.2 Ωm), and sharply increasing sonic velocity (>2200 m/s). Because this subunit is directly in contact with the basement rock below, it is possible that some alteration of the sediment has occurred, as observed in the core samples previously obtained at this site. Therefore, this subunit is interpreted to represent the altered red clay samples identified during Expeditions 322 and 333 in Holes C0012A and C0012G (Expedition 322 Scientists, 2010c; Expedition 333 Scientists, 2012c).

Basement rock (530.3–710.0 mbsf)

Within the basement section, gamma ray values are low (<60 gAPI), which is typical of basaltic rock (Barr et al., 2002; Bartetzko et al., 2001) recovered during Expeditions 322 and 333 (Expedition 322 Scientists, 2010c; Expedition 333 Scientists, 2012c). Therefore, the reference gamma ray baseline for this section was set at 18 gAPI to reflect the average value (Fig. **F7**). Based on this, the basement was divided into two logging units (Table **T2**). Subunits in logging Unit VII were defined based on large-scale changes in the resistivity and sonic velocity logs, which are positively correlated. Subunits VIIA and VIIB may correspond to the igneous Units I and II defined in cores (igneous Unit I: pillow lavas; igneous Unit II: sheet flows with pillow lava interlayers [Expedition 333 Scientists, 2012c]); however, without more compositional information from logs (e.g., neutron density logs, photoelectric factor, or spectral gamma ray), a detailed lithologic interpretation of the basement is not possible.

Logging Unit VII (530.3–626.6 mbsf)

Through logging Unit VII, the gamma ray log exhibits significant variation with depth (Fig. **F7**). Immediately below the sediment/basement contact (530.3 mbsf), gamma ray values decrease from ~90 to ~20 gAPI. At 536.7 mbsf, gamma ray values become constant with only minor (±5 gAPI) fluctuations to ~559.4 mbsf, where gamma ray values spike to ~35 gAPI coincident with drops in resistivity and sonic velocity to 1.3 Ωm and 3500 m/s, respectively. At 562.12 mbsf, gamma ray values increase from ~30 to 45 gAPI before gradually decreasing to ~15 gAPI by 575.57 mbsf. Gamma ray values show a minor increase to ~25–30 gAPI between 575.57 and 589.01 mbsf before another increase to ~50 gAPI at 595 mbsf. Below 595 mbsf, gamma ray values gradually decrease to ~15 gAPI at 607 mbsf before gradually increasing to ~40 gAPI at 624.62 mbsf. A decrease in gamma ray values to ~15 gAPI over a 2 m interval marks the base of logging Unit VII at 626.6 mbsf. These fluctuations may represent volcaniclastic sediment intercalated between lava flows or varying alterations to the basalt, as identified from petrologic investigation of core samples (Expedition 333 Scientists, 2012c).

Three subunits have been defined within logging Unit VII based on fluctuations in the resistivity and sonic velocity logs (Fig. **F7;** Table **T2**). Subunit VIIA (530.3–572.9 mbsf) exhibits gradually decreasing resistivity (from 3.0 to 1.6 Ωm), whereas velocity remains fairly constant (~3500 ± 200 m/s) to 564.6 mbsf, where it drops to ~3000 m/s (±300 m/s). At 572.9 mbsf, both resistivity and sonic velocity increase over a 7 m interval to ~20 Ωm and ~4900 m/s, respectively. Throughout Subunit VIIB (572.9–604.1 mbsf), resistivity and sonic velocity remain high (~30 Ωm and 4900 m/s, respectively). At 595.5–596.5 mbsf, low spikes in both resistivity (~6.5 Ωm) and sonic velocity (~3400 m/s) correspond to a high in gamma ray values (~50 gAPI), possibly indicating a highly altered pillow basalt or a volcaniclastic sediment horizon. The base of Subunit VIIB is placed where resistivity and sonic velocity drop back to lower values similar to those in Subunit VIIA. From 604.1 to 613.17 mbsf, resistivity remains constant at ~3.2 Ωm (±0.5 Ωm) and sonic velocity remains constant at ~3200 m/s (±300 m/s), characterizing the up-

per part of Subunit VIIC. There is an increase in both resistivity and sonic velocity to 7.0 Ωm and 4400 m/s, respectively, between 613.17 and 614.0 mbsf. Between 614.0 and 619.14 mbsf, resistivity gradually decreases to ~5.0 Ωm, and resistivity then remains constant through the rest of Subunit VIIC. Sonic velocity exhibits an overall decrease (to ~4100 m/s) to the base of Subunit VIIC.

Logging Unit VIII (626.6–710.0 mbsf)

Below 626.6 mbsf, gamma ray values become consistently low (~15 gAPI) with only minor fluctuations (±5 gAPI). Resistivity exhibits some variability with depth but remains high relative to all the other units (Fig. F4). From 626.6 to 632.0 mbsf, resistivity and sonic velocity gradually increase to ~8.5 Ωm and ~4700 m/s, respectively. From 632.0 to 656.5 mbsf, resistivity remains consistently around >8.5 Ωm with minor fluctuations (±4.0 Ωm). Sonic velocity decreases over the same depth interval (632.0–656.5 mbsf) from ~4700 to 4000 m/s. A shift to a higher average resistivity (~15 Ωm) is observed from 656.5 to 684.4 mbsf with fluctuations between 7 and 25 Ωm, reaching a high (~25 Ωm) around 682.0–684.0 mbsf. At 684.5 mbsf, resistivity returns to an average value of 8.5 Ωm and maintains low variability to the base of the hole (710 mbsf), with a wide spike to ~20 Ωm at 700 mbsf. Below 656.5 mbsf, sonic velocity exhibits two increasing profiles. From 656.5–665.9 mbsf, sonic velocity increases from ~4000 to 5300 m/s before sharply decreasing to ~4000 m/s at 668.7 mbsf. Another gradual increase to ~4800 m/s is observed to 683.88 mbsf before sonic velocity decreases to ~3750 m/s at 687.0 mbsf. There are no sonic velocity measurements below this depth because of the placement of the sonicVISION tool in the BHA (see the "Methods" chapter [Strasser et al., 2014a]). In the absence of further logging data (e.g., density) and no core data, no subunit classification was applied to this logging unit.

Physical properties

Estimation of porosity and bulk density from resistivity

Porosity was estimated using Archie's law (Archie, 1947; see the "Methods" chapter [Strasser et al., 2014a]). Seawater electrical resistivity was calculated using the temperature profile that was estimated for Site C0012 during Expedition 333. The temperature at the seafloor was estimated to be 2.85°C, with an average thermal gradient of 135°C/km (Expedition 333 Scientists, 2012c). Archie's law parameters were found by fitting the Archie equation to reliable resistivity measurements of discrete samples (conducted at 2 kHz) and moisture and density (MAD)-derived porosity measurements taken during Expedition 333 on sediment in the upper 180 m of Site C0012 (Expedition 333 Scientists, 2012b). Resistivity and MAD-derived porosity measurements taken at Site C0012 during Expedition 322 were not used in the Archie's law fit because the resistivity measurements were taken at a current frequency of 25 kHz (Expedition 322 Scientists, 2010a). The Schlumberger geoVISION tool measures resistivity at the bit at a current frequency of 1.5 kHz (Bonner et al., 1996), making use of the Expedition 333 data appropriate. The parameters that best fit the data are $a = 1$ and $m = 2.95$ with a coefficient of determination (R^2) of 0.78 (Fig. F8). Archie parameters employed at Site C0002 ($a = 1$ and $m = 2.4$) (Expedition 314 Scientists, 2009; see the "Site C0002" chapter [Strasser et al., 2014b]) are similar to those estimated here for Site C0012. These parameters are applied to the entire drilled section of Hole C0012H; thus, the a and m values do not account for lithologic variations with depth or the presence of igneous basement below 530.3 mbsf. Bulk density was estimated from the resistivity-derived porosity using a grain density (ρ_g) value of 2.67 g/cm^3. This grain density value is an average (with a standard deviation of 0.12 g/cm^3) of all the MAD-derived grain densities for sediment above the igneous basement measured during Expeditions 322 and 333 (Expedition 322 Scientists, 2010c; Expedition 333 Scientists, 2012c).

Resistivity-derived porosity and bulk density depth trends are shown in Figure F4. Porosity is somewhat scattered in the upper 70 m but averages 71% ± 2%. Porosity decreases linearly from 72% to 58% from 70 to 107 mbsf and then increases to 66% at 123 mbsf. Between 123 mbsf and the base of Unit II (188.1 mbsf), porosity decreases to 54% and then remains generally constant to 372.1 mbsf. Within Subunit IVB (372.1–403.3 mbsf), there is a slight negative excursion in porosity, decreasing to 49% at ~388 mbsf before increasing to 54% at the base of Unit IV (403.3 mbsf). Within Units V and VI (403.3–530.3 mbsf), porosity values decrease gradually from 54% to 45% at the base of Unit VI (530.3 mbsf) before decreasing precipitously to <30% at the top of Unit VII (530.3 mbsf). This rapid decrease corresponds to the upper surface of the basement. Within Unit VII (530.3–626.6 mbsf), porosity increases gradually to 38% at 570 mbsf before decreasing suddenly to 17% at 578 mbsf, increasing rapidly to 29% at 604 mbsf, and finally decreasing to 23% at the base of Unit VII (626.6 mbsf). Porosity is generally scattered at ~20% within Unit VIII (626.6–710 mbsf), reaching as low as 15% between 665 and 683 mbsf and 23% at the base of Hole C0012H at 710 mbsf. Note that esti-

mated porosity in the basement units (VII and VIII) are subject to errors because of the assumed constant values for *a* and *m* throughout the hole.

Trends in resistivity-derived bulk density mirror those described above for the resistivity-derived porosity because reported bulk density values are a mathematical manipulation of the derived porosity values (Fig. F4). Generally, bulk density increases from ~1.4 g/cm^3 at the seafloor to 1.7 g/cm^3 at 107.2 mbsf (within Unit I). Bulk density decreases to 1.6 g/cm^3 at 123 mbsf before generally increasing to 1.9 g/cm^3 at the base of Unit VI (530.3 mbsf). Within the basement (Units VII and VIII; 530.3–710 mbsf), bulk density averages 2.3 ± 0.1 g/cm^3 but is subject to the same errors as resistivity-derived porosity in the basement units.

The resistivity-derived porosity log is plotted for comparison along with MAD-derived porosity measurements taken during Expeditions 322 and 333 (Expedition 322 Scientists, 2010c; Expedition 333 Scientists, 2012c). The resistivity-derived estimate maintains good visual agreement with MAD-derived measurements to ~186 mbsf, where they become increasingly offset (Fig. F9). Below 186 mbsf, the resistivity-derived values are consistently higher than the MAD-derived values, with the offset $\Delta\phi = \phi_{MAD} - \phi_{resistivity}$ between the two reaching a maximum of about $\Delta\phi = -0.2$ (relative to the resistivity-derived values) near the base of the sedimentary section at 530.3 mbsf. This difference could be due to lithologic changes that are not captured by the Archie's law model, for which we assumed constant values of *a* and *m*. Another possible explanation is the observed salinity increase with depth at Site C0012 (Expedition 322 Scientists, 2010c); although this decreases the pore fluid resistivity, it would not account for the full offset. For example, a salinity of ~4.0% was measured from interstitial water at the base of the sedimentary section at Site C0012 during Expedition 322 (Expedition 322 Scientists, 2010c). Using the thermal gradient reported above, the temperature at 530 mbsf is ~62°C. Under these conditions, seawater resistivity is ~0.23 Ωm, compared to ~0.27 Ωm for seawater with a salinity of 35 (Schlumberger, 2009). From Archie's law (see the **"Methods"** chapter [Strasser et al., 2014a]), increasing the salinity from 3.5% to 4.0% corresponds to an ~0.02 decrease in porosity, which is about an order of magnitude less than the observed difference between the resistivity- and MAD-derived porosity values at 530 mbsf.

Resistivity image analysis

The statically normalized shallow, medium, and deep button resistivity images were the primary images used for structural and geomechanical analyses. Three different resistivity ranges were selected to normalize the data: 0.5–1.5 Ωm for the Shikoku Basin sediment and 0–10 or 2–50 Ωm for basement rock. In the absence of a caliper measurement, the bit diameter was used as the borehole diameter and assumed to be constant. Therefore, all reported dip angles should be considered as a maximum bound. Observations are summarized separately for the Shikoku Basin sediment and basement rock.

Shikoku Basin sediment (logging Units I–VI)

Generally, bedding dips are gentle-to-moderate (10°–30°). The dominant dip direction is bipolar, with strong clustering in both west–northwest and east–northeast directions (Fig. F4). Overall, there is low variability in sediment resistivity throughout the entire section, although the number of visible bedding planes increases at depths >330 mbsf as a direct result of the increase in resistivity contrast between adjacent beds (Fig. F6). The average fracture density is <1 per 10 m, although logging Unit VI has a higher than average concentration of ~3 per 10 m (463.5–530.3 mbsf).

Only six bedding planes were visible in logging Unit I, with variable dip direction from north through to west and moderate dip angle (20°–28°; Fig. F6). It is possible that there were more bedding planes with dip angles close to horizontal, but these were not picked, as they were impossible to distinguish from data overlap artifacts caused by tool bounce, especially in regions of high stick-slip (**"Data quality"**).

Logging Units III and IV have strong evidence for opposite bedding dip directions (Fig. F4). Between 188.1 and 250.0 mbsf, dip direction is to the west, and between 333.0 and 372.1 mbsf, dip direction is to the east. There is a lack of clear bedding planes between 250.0 and 333.0 mbsf (Fig. F6). In this lower ~80 m section of Unit III, only two bedding planes are observed, both dipping gently (~18°) to the southeast. Fractures in Unit III mostly dip toward the east, with a large range of dip angles (18°–80°). Several high-angle (>70°) north- or south-dipping fractures are also observed.

Bedding planes in logging Unit IV dip to the east, with dip angles ranging from 15° to 25°. Logging Unit V has the most variable bedding plane dip directions (Fig. F4), although dip angles were predominantly gentle to moderate (10°–30°). No fractures were observed in the upper section of logging Unit V (403.3–437.0 mbsf), and only five low-angle fractures (<22°) were picked in the lower section (437.0–463.5 mbsf; Fig. F6). Logging Unit VI demonstrates two strong trends in dip direction: northwest to west from 463.5 to 497.0 mbsf and east to southeast from

497.0 to 530.3 mbsf (Figs. F4, F6). Well-defined bedding planes were observed in logging Subunit VIC (526.7–530.3 mbsf), with dip angles of 20°–38° to the southeast. A high number of fractures were also identified in logging Unit VI, with characteristically medium to high dip angles (40°–75°) and variable dip directions that do not appear to correlate with the bedding planes (Fig. F6).

Basement (logging Units VII–VIII)

An irregular contact is observed at 530.3 mbsf between the base of the Shikoku Basin sediment (logging Unit VI) with a low resistivity (<1.5 Ωm) and the top of the basement (logging Unit VII) with a higher resistivity (>3 Ωm) (Fig. F10A). Within the ~180 m section of basement that was logged, a wide variety of textures and fracture patterns can broadly be summarized as follows (Fig. F10):

- Mottled texture, distinct from other regions of clear fracturing;
- "Turtleshell" texture, approximately circular regions of high-resistivity "clasts" within a lower resistivity network; and
- Zones of homogeneous background resistivity, often with subvertical fractures (either individual or anastomosing).

The mottled texture could be interpreted as zones containing a multitude of small fractures or, alternatively, as material that is chaotic or irregular, perhaps representing pillow breccia or hyaloclastite. A third interpretation could be different alteration of the basalt. This mottled texture is often observed in conjunction with, or directly overlying, zones of turtleshell texture. The turtleshell texture may also result from a complex fracture network, but this texture differs from other fractured zones by the presence of approximately circular resistive clasts within a lower resistivity network (Fig. F10B, F10E). It is possible that this texture represents various sized pillow basalts. The homogeneous high-resistivity zones containing subvertical fractures may represent sheet flows (Fig. F10C, F10D). Table T3 summarizes the observed textures and their preliminary interpretation according to their depth range and includes the thickness and range of resistivity for each occurrence. To compare intervals of different basement textures with variations in other LWD data, refer to Figure F7.

Both planar and subvertical fractures were picked (Fig. F7). The lower resistivity networks around the pillow basalts were also picked as fractures to check for any correlation between changes in ring/bit resistivity and sonic velocity and the number of fractures or regions of low resistivity in the images.

Logging Subunit VIIA generally has textural variations every 5 m or less, with the exception of two ~10 m thick regions of pillow basalts at 537.5–545.7 and 557.0–566.6 mbsf (Fig. F10B; Table T3). The fracture density within logging Subunit VIIA is ~10 per 10 m, and the subvertical fractures are relatively wide (~0.05 m) and sinuous. Logging Subunit VIIB is dominated by two large (19.0 and 7.2 m thick) zones of relatively high, homogeneous background resistivity with thinner subvertical fractures (~0.02 m) compared to logging Subunit VIIA. These zones still have a moderate number of fractures (~5 per 10 m), including a steeply dipping (~75°), low-resistivity (<7 Ωm) fracture that is ~0.1 m wide (Fig. F10C). Logging Subunit VIIC has a mixture of all three textures (Fig. F10D), although resistivity is generally higher than that of logging Subunit VIIA, reflecting its lower fracture content (Fig. F7).

Logging Unit VIII has an average resistivity of ~10 Ωm, although it contains the same textural features as logging Subunit VIIC. At ~684 mbsf, a sharp decrease in resistivity from ~50 to <10 Ωm correlates with a sharp transition from a sheet flow to pillow basalts (Fig. F10E). Similar basal surfaces can be observed elsewhere within logging Unit VIII (and logging Unit VII to a lesser extent), although these are less distinctive. The repetition of these textures, with pillows and mottled regions overlying sheet flows with sharp basal surfaces, suggests that there have been multiple cycles of pillow basalt and sheet flows, with each set having a variable combined thickness, ranging from ~3 to >25 m (Table T3).

Borehole breakouts

Four breakouts were observed in the Shikoku Basin sediment between 424.5 and 518.6 mbsf. Three of the breakouts occurred in logging Unit V, with heights ranging between 0.45 and 0.85 m and widths of 30° to 60° that were often uneven between the pairs (Fig. F11A). The breakout in logging Unit VI was more diffuse and taller (~1.9 m) than those seen in logging Unit V. Orientations of the breakouts were used to estimate the direction of principal horizontal stress (S_{HMAX}). The uppermost and lowermost breakouts (at 424.8 and 517.7 mbsf) agree with a north–south S_{HMAX} orientation, whereas the central two breakouts (at 442.6 and 446.6 mbsf) both demonstrate a northeast–southwest S_{HMAX} orientation. Drilling-induced tensile fractures (DITFs) were observed in basement rock (logging Units VII and VIII). A clear example of a pair (i.e., 180° apart) of DITFs

can be observed between 658.0 and 678.0 mbsf (Fig. F11B).

Core-log-seismic integration

Hole C0012H is located ~30 m southeast of Hole C0012A; ~40 m south of Holes C0012C–C0012E; and ~40 m east of Holes C0012F and C0012G (Expedition 322 Scientists, 2010c; Expedition 333 Scientists, 2012c). Cores recovered from Holes C0012A–C0012E provided detailed lithologic information for the Shikoku Basin sedimentary sequence from 0 to 530 mbsf. Intermittent recovery from Holes C0012A, C0012E, C0012F, and C0012G also provided some lithologic information about the underlying basement rock of the Philippine Sea plate starting at 530 mbsf.

The upper and lower Shikoku Basin strata of Ike et al. (2008) were correlated with seismic Units A–C and D–F identified on Institute for Research on Earth Evolution (IFREE) 3-D prestack depth migration (PSDM) (Park et al., 2008) In-line 95 by Expedition 322 Scientists (2010c). Seismic Unit G represents the basement, and although some samples were recovered from coring during Expeditions 322 and 333, correlation with logging data is not attempted here. Instead, the seismic and lithologic unit correlation (predominantly Hole C0012A) is revisited with integration of LWD data from Hole C0012H. Mismatches between the depths of the seismic unit boundaries and the logging or lithologic unit boundaries are predominantly a result of errors in the velocity field used to generate the 3-D PSDM data. Figure F12 presents an overview of the correlation between the LWD, seismic, and core data. The results are also summarized in Table T4.

Seismic Units A and B were first defined at Site C0011 and then extrapolated to Site C0012 (Expedition 322 Scientists, 2010c). The boundary between the two seismic units is unclear at Site C0012 but is interpreted to be at ~70 mbsf. The seismic character of the A–B interval (0–120 mbsf) exhibits low-amplitude reflectivity with some irregular and discontinuous reflectors. This interval, cored in Hole C0012A, shows a dominant lithology of hemipelagic mudstone with a few volcanic ash/tuff beds, although no cores were taken from 0 to 60 mbsf. The shallow section was cored in Holes C0012C and C0012D (Expedition 333 Scientists, 2012c), where a large number of thin volcanic ash/tuff beds were recovered within the background hemipelagic mudstone. The change in abundance of volcanic ash/tuff layers, many within the topmost 60 mbsf and few from 60 to 150 mbsf (Fig. F12), could represent the seismic Unit A/B boundary. The corresponding logging unit defined in Hole C0012H (logging Unit I, 0–144.3 mbsf) does include a slight increase in average gamma ray value at ~70 mbsf, but the correlation is uncertain.

Logging Unit II (144.3–188.1 mbsf) has a greater variability in gamma ray values (between 35 and 95 gAPI). The baseline for Hole C0012H was set at 95 gAPI (see "Logging while drilling"), so the variations represent lows with a characteristic thickness of ~5 m. This interval corresponds to lithologic Unit II in Hole C0012A, which contains several volcanic sandstone beds (each ~5 m thick), and seismic Unit C, which contains a series of high-amplitude, continuous reflections. The top of this section is also marked by a small step increase in sonic velocity in Hole C0012H from 1650 to 1750 m/s (Fig. F4). High density values and *P*-wave velocities (1.9 g/cm^3 and 2000 m/s, respectively) were also reported from Hole C0012A sandstone samples (Expedition 333 Scientists, 2012c). The density and velocity measurements from both cores and logging data show a good correlation with the observation of strong reflections between 120 and 200 mbsf in the IFREE seismic data (Fig. F12).

Lithologic Units III and IV (215–415 mbsf) comprise hemipelagic mudstone and hemipelagic mudstone with interbedded siltstone turbidites, respectively. Seismic Unit D at the corresponding depth interval of 200–405 mbsf is transparent (i.e., no strong reflections), indicating no major impedance contrasts, as would be expected for a hemipelagic section. There is evidence in the LWD data for the increasing number of siltstone turbidites between 330 and 415 mbsf (lithologic Unit IV) from spikes in gamma ray to low values (~30 gAPI) within logging Subunit IVA (339.6–372.1 mbsf). In contrast, no distinction was found in Hole C0012A cores to match the high gamma ray (>100 gAPI) and resistivity (>1 Ωm) of logging Subunit IVB.

Logging Units V and VI (403.3–530.3 mbsf) show a similar pattern of increasing gamma ray values with increasing depth from 75 to 100 and 65 to 90 gAPI, respectively (Fig. F12). Lithologic Unit V (415.58–528.51 mbsf) contains a series of sandstone turbidites overlying a series of volcanic sandstones, all within a background of hemipelagic mudstone. An increase in the ratio of mudstone to volcanic sandstone or sandstone turbidite with depth could explain the observed increases in gamma ray. Although the lithologic column does not match this hypothesis, incomplete core recovery may have resulted in some interpolation, especially at the base of lithologic Unit V (Expedition 322 Scientists, 2010c). Seismic Unit E contains a series of strong reflections be-

tween 405 and 530 mbsf, corroborating the observation of interbedded sandstones/turbidites and hemipelagic mudstone.

Lithologic Unit VI (~530–537 mbsf) was identified as a thermal alteration of the hemipelagic mudstone, resulting from contact with the basement rock of lithologic Unit VII (seismic Unit G, logging Unit VII). Although not picked as a discrete logging unit, there is evidence for a 3–4 m thick layer with *P*-wave velocities of ~2050 m/s directly overlying the basement in Hole C0012H. Finally, the basement seismic character is a consistently low frequency below ~530 mbsf.

References

Archie, G.E., 1947. Electrical resistivity—an aid in core analysis interpretation. *AAPG Bull.,* 31(2):350–366.

Barr, S.R., Révillon, S., Brewer, T.S., Harvey, P.K., and Tarney, J., 2002. Determining the inputs to the Mariana Subduction Factory: using core-log integration to reconstruct basement lithology at ODP Hole 801C. *Geochem., Geophys., Geosyst.,* 3(11):8901–8925. **doi:10.1029/2001GC000255**

Bartetzko, A., Pezard, P., Goldberg, D., Sun, Y.-F., and Becker, K., 2001. Volcanic stratigraphy of DSDP/ODP Hole 395A: an interpretation using well-logging data. *Mar. Geophys. Res.,* 22(2):111–127. **doi:10.1023/A:1010359128574**

Bonner, S., Fredette, M., Lovell, J., Montaron, B., Rosthal, R., Tabanou, J., Wu, P., Clark, B., Mills, R., and Williams, R., 1996. Resistivity while drilling—images from the string. *Oilfield Rev.,* 8(1):4–19. **http://www.slb.com/~/media/Files/resources/oilfield_review/ors96/spr96/composite.ashx**

Expedition 314 Scientists, 2009. Expedition 314 Site C0002. *In* Kinoshita, M., Tobin, H., Ashi, J., Kimura, G., Lallemant, S., Screaton, E.J., Curewitz, D., Masago, H., Moe, K.T., and the Expedition 314/315/316 Scientists, *Proc. IODP,* 314/315/316: Washington, DC (Integrated Ocean Drilling Program Management International, Inc.). **doi:10.2204/iodp.proc.314315316.114.2009**

Expedition 322 Scientists, 2010a. Methods. *In* Saito, S., Underwood, M.B., Kubo, Y., and the Expedition 322 Scientists, *Proc. IODP,* 322: Tokyo (Integrated Ocean Drilling Program Management International, Inc.). **doi:10.2204/iodp.proc.322.102.2010**

Expedition 322 Scientists, 2010b. Site C0011. *In* Saito, S., Underwood, M.B., Kubo, Y., and the Expedition 322 Scientists, *Proc. IODP,* 322: Tokyo (Integrated Ocean Drilling Program Management International, Inc.). **doi:10.2204/iodp.proc.322.103.2010**

Expedition 322 Scientists, 2010c. Site C0012. *In* Saito, S., Underwood, M.B., Kubo, Y., and the Expedition 322 Scientists, *Proc. IODP,* 322: Tokyo (Integrated Ocean Drilling Program Management International, Inc.). **doi:10.2204/iodp.proc.322.104.2010**

Expedition 333 Scientists, 2012a. Expedition 333 summary. *In* Henry, P., Kanamatsu, T., Moe, K., and the Expedition 333 Scientists, *Proc. IODP,* 333: Tokyo (Integrated Ocean Drilling Program Management International, Inc.). **doi:10.2204/iodp.proc.333.101.2012**

Expedition 333 Scientists, 2012b. Methods. *In* Henry, P., Kanamatsu, T., Moe, K., and the Expedition 333 Scientists, *Proc. IODP,* 333: Tokyo (Integrated Ocean Drilling Program Management International, Inc.). **doi:10.2204/iodp.proc.333.102.2012**

Expedition 333 Scientists, 2012c. Site C0012. *In* Henry, P., Kanamatsu, T., Moe, K., and the Expedition 333 Scientists, *Proc. IODP,* 333: Tokyo (Integrated Ocean Drilling Program Management International, Inc.). **doi:10.2204/iodp.proc.333.105.2012**

Heki, K., 2007. Secular, transient, and seasonal crustal movements in Japan from a dense GPS array: implication for plate dynamics in convergent boundaries. *In* Dixon, T.H., and Moore, J.C. (Eds.), *The Seismogenic Zone of Subduction Thrust Faults:* New York (Columbia Univ. Press), 512–539.

Ike, T., Moore, G.F., Kuramoto, S., Park, J.-O., Kaneda, Y., and Taira, A., 2008. Variations in sediment thickness and type along the northern Philippine Sea plate at the Nankai Trough. *Isl. Arc,* 17(3):342–357. **doi:10.1111/j.1440-1738.2008.00624.x**

Park, J.-O., Tsuru, T., No, T., Takizawa, K., Sato, S., and Kaneda, Y., 2008. High-resolution 3D seismic reflection survey and prestack depth imaging in the Nankai Trough off southeast Kii Peninsula. *Butsuri Tansa,* 61:231–241. (in Japanese, with abstract in English)

Rider, M., 2002. *The Geological Interpretation of Well Logs* (2nd ed.): Sutherland, Scotland (Rider-French Consulting Ltd.).

Schlumberger, 2009. *Log Interpretation Charts:* Houston (Schlumberger).

Seno, T., Stein, S., and Gripp, A.E., 1993. A model for the motion of the Philippine Sea plate consistent with NUVEL-1 and geological data. *J. Geophys. Res.: Solid Earth,* 98(B10):17941–17948. **doi:10.1029/93JB00782**

Strasser, M., Dugan, B., Kanagawa, K., Moore, G.F., Toczko, S., Maeda, L., Kido, Y., Moe, K.T., Sanada, Y., Esteban, L., Fabbri, O., Geersen, J., Hammerschmidt, S., Hayashi, H., Heirman, K., Hüpers, A., Jurado Rodriguez, M.J., Kameo, K., Kanamatsu, T., Kitajima, H., Masuda, H., Milliken, K., Mishra, R., Motoyama, I., Olcott, K., Oohashi, K., Pickering, K.T., Ramirez, S.G., Rashid, H., Sawyer, D., Schleicher, A., Shan, Y., Skarbek, R., Song, I., Takeshita, T., Toki, T., Tudge, J., Webb, S., Wilson, D.J., Wu, H.-Y., and Yamaguchi, A., 2014a. Methods. *In* Strasser, M., Dugan, B., Kanagawa, K., Moore, G.F., Toczko, S., Maeda, L., and the Expedition 338 Scientists, *Proc. IODP,* 338: Yokohama (Integrated Ocean Drilling Program). **doi:10.2204/iodp.proc.338.102.2014**

Strasser, M., Dugan, B., Kanagawa, K., Moore, G.F., Toczko, S., Maeda, L., Kido, Y., Moe, K.T., Sanada, Y., Esteban, L., Fabbri, O., Geersen, J., Hammerschmidt, S., Hayashi, H., Heirman, K., Hüpers, A., Jurado Rodriguez, M.J., Kameo, K., Kanamatsu, T., Kitajima, H., Masuda, H., Milliken, K., Mishra, R., Motoyama, I., Olcott, K., Oohashi, K.,

Pickering, K.T., Ramirez, S.G., Rashid, H., Sawyer, D., Schleicher, A., Shan, Y., Skarbek, R., Song, I., Takeshita, T., Toki, T., Tudge, J., Webb, S., Wilson, D.J., Wu, H.-Y., and Yamaguchi, A., 2014b. Site C0002. *In* Strasser, M., Dugan, B., Kanagawa, K., Moore, G.F., Toczko, S., Maeda, L., and the Expedition 338 Scientists, *Proc. IODP,* 338: Yokohama (Integrated Ocean Drilling Program). **doi:10.2204/iodp.proc.338.103.2014**

Underwood, M.B., Saito, S., Kubo, Y., and the Expedition 322 Scientists, 2010. Expedition 322 summary. *In* Saito, S., Underwood, M.B., Kubo, Y., and the Expedition 322 Scientists, *Proc. IODP,* 322: Tokyo (Integrated Ocean Drilling Program Management International, Inc.). **doi:10.2204/iodp.proc.322.101.2010**

Publication: 13 January 2014
MS 338-104

Figure F1. Regional location map showing Site C0012 in context of the NanTroSEIZE project sites. Box = region with 3-D seismic data, red = Expedition 338 sites, blue = NanTroSEIZE Stage 1 and 2 sites, yellow arrows = estimated far-field vectors between Philippine Sea plate and Japan (Seno et al., 1993; Heki, 2007), stars = epicenter locations of 1944 and 1946 tsunamigenic earthquakes.

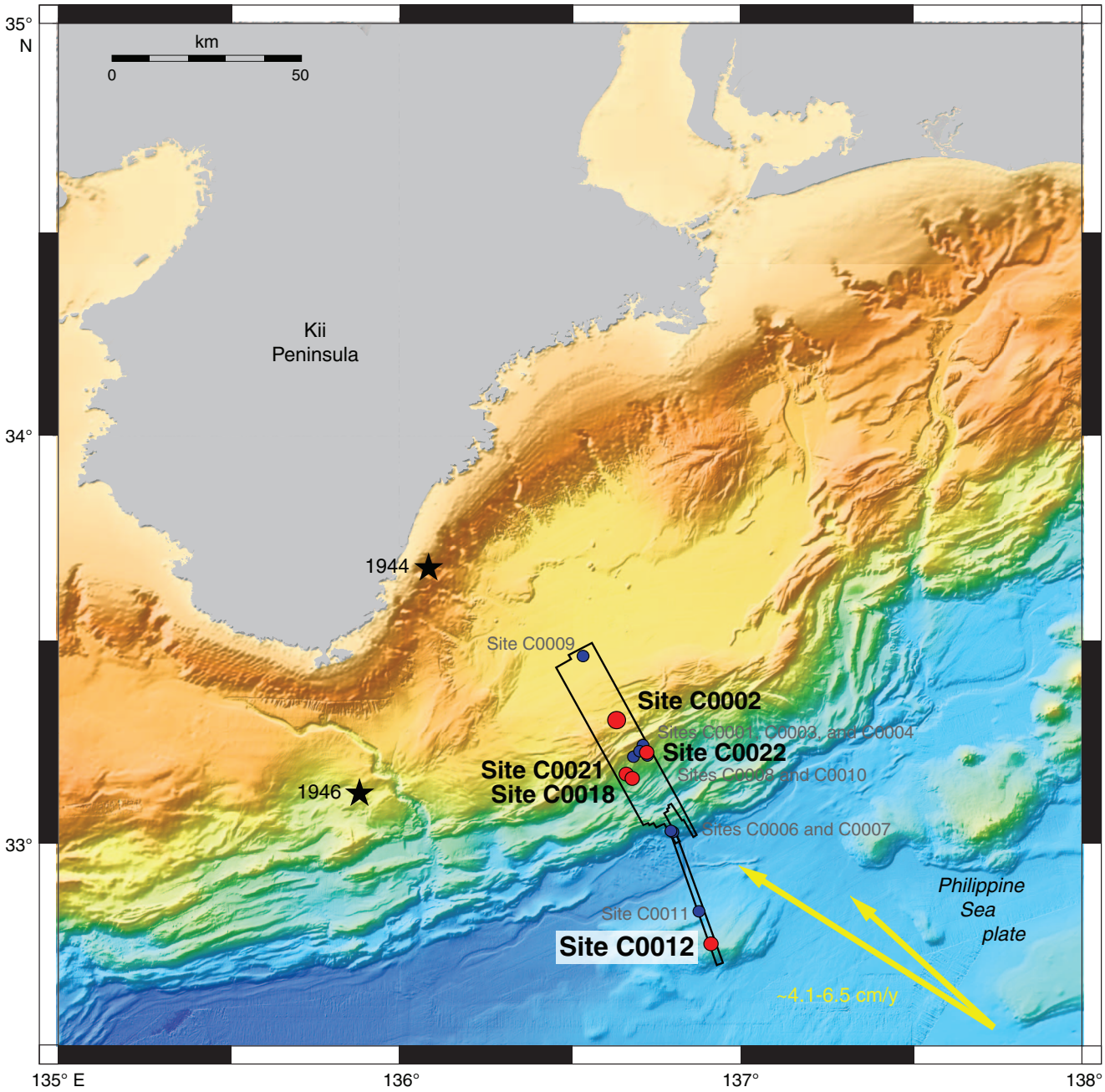

Figure F2. Location of Sites C0011 and C0012 plotted along Institute for Research on Earth Evolution (IFREE) seismic In-line 95. CDP = common depth point. VE = vertical exaggeration.

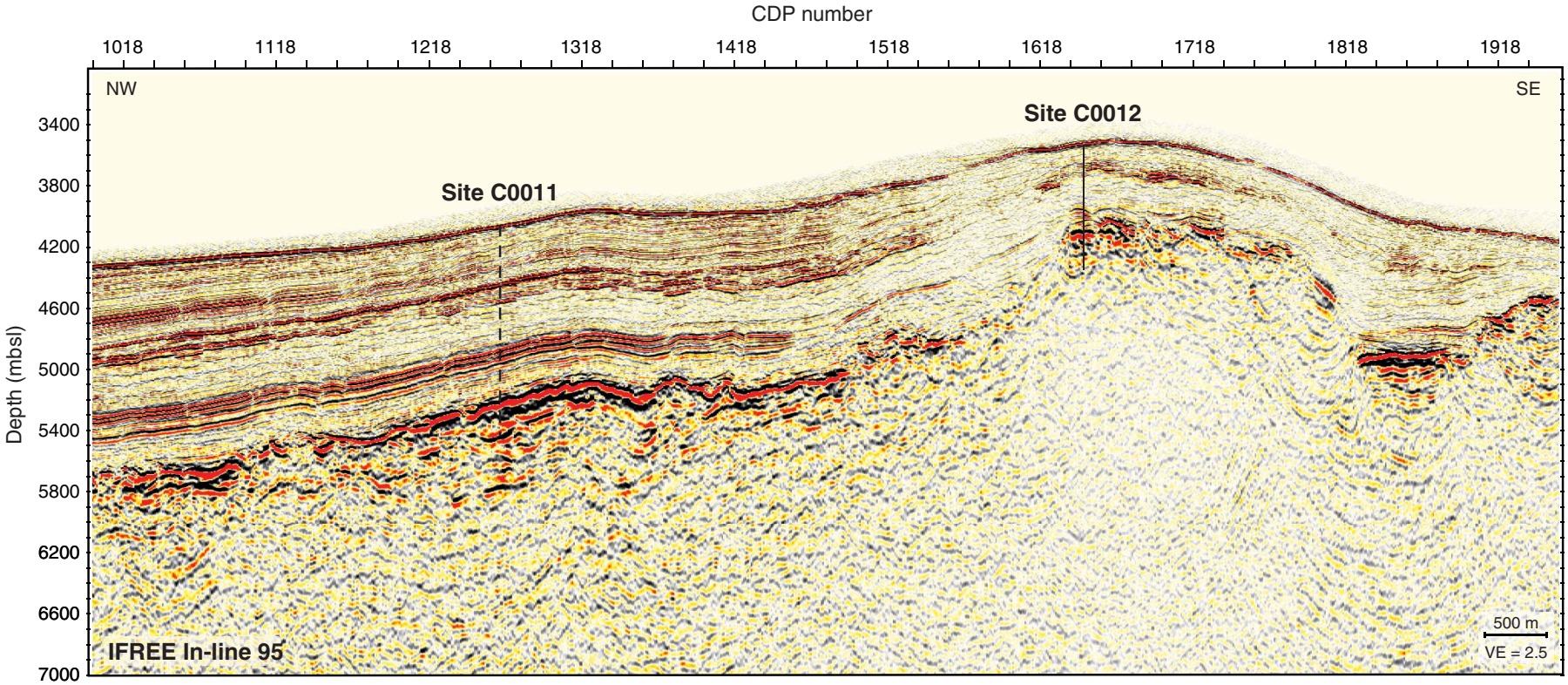

Figure F3. Selection of MWD logs and drilling parameters, Hole C0012H.

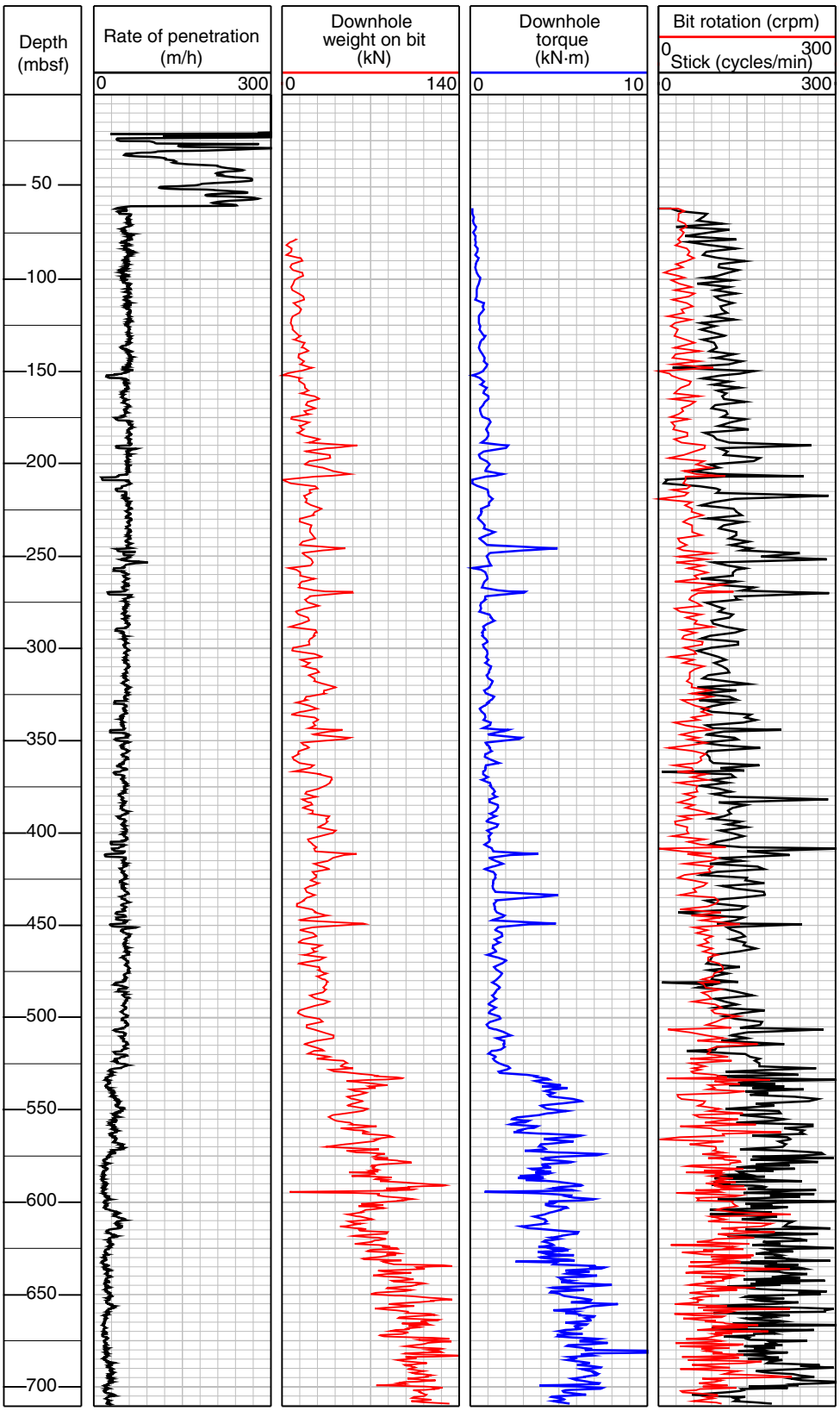

Figure F4. Composite plot of LWD data for Hole C0012H, showing gamma ray, seismic data, resistivity, sonic velocity, deep button resistivity image, bedding and fracture dips, resistivity-derived bulk density and porosity, and logging units. The resistivity image has been normalized for the basement separate to the Shikoku Basin section.

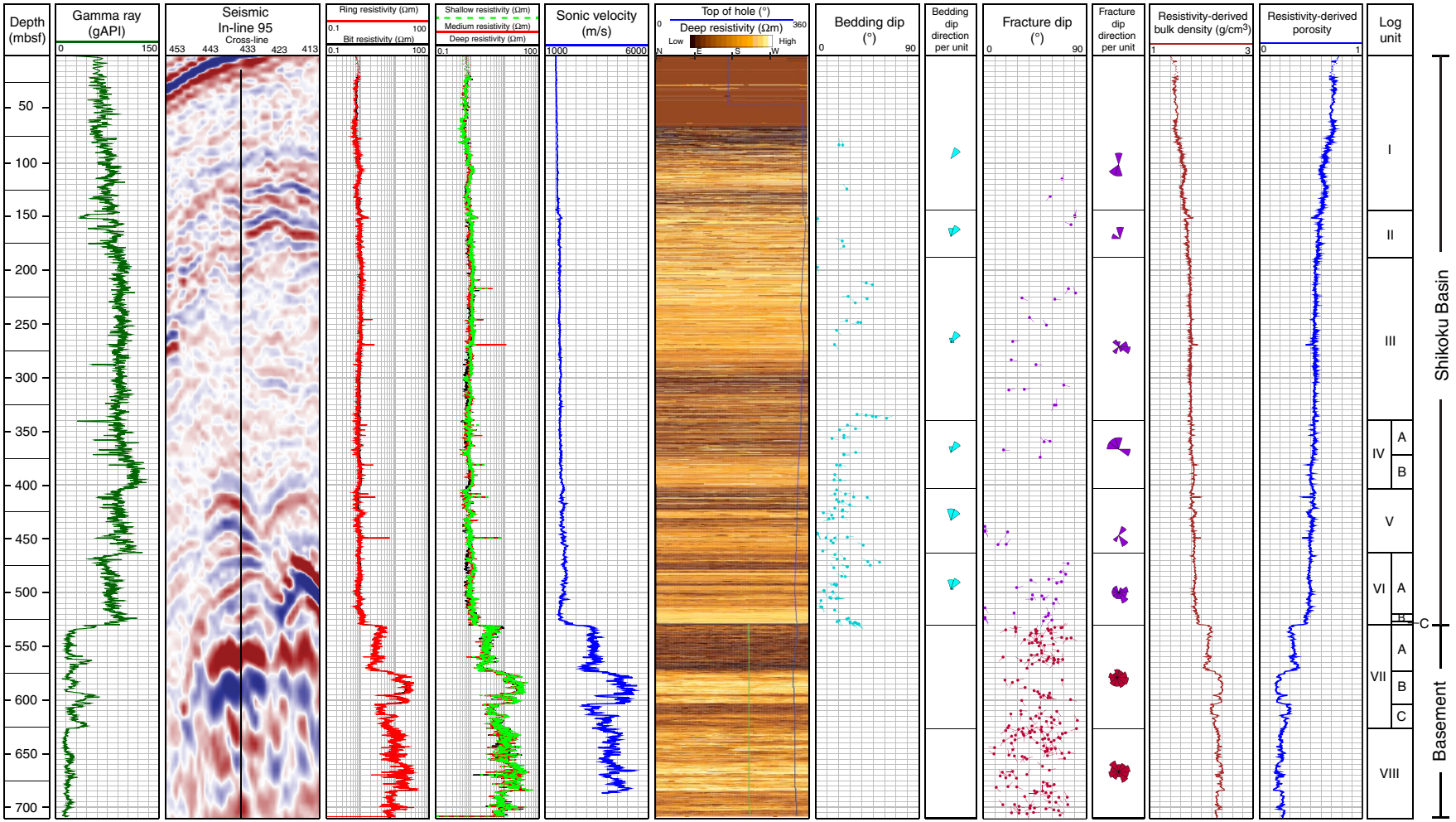

Figure F5. Box and whisker plots of logging units for gamma ray, resistivity, and sonic velocity, illustrating the large change in values between Shikoku Basin sediment and basement rock. The box bounds represent the 25th and 75th percentile values per unit, and the error bars reach the maximum and minimum values recorded, excluding any identified outliers.

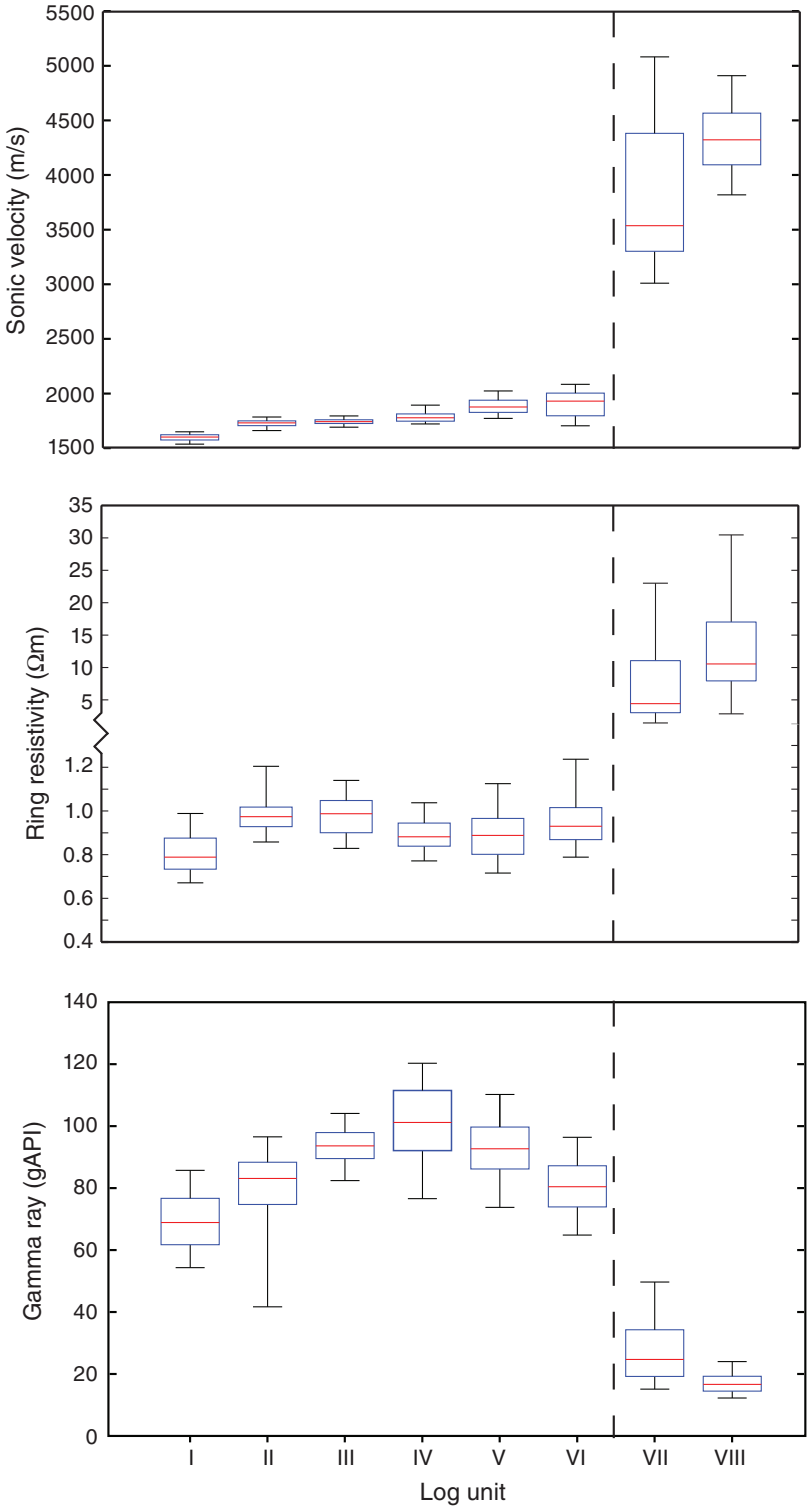

Figure F6. Composite plot of the LWD data for the sediment section (0–530.3 mbsf), showing gamma ray, interpreted lithology (Interp. lith.), logging units, resistivity, sonic velocity, bedding and fracture dips, and deep button resistivity image. The gamma ray baseline was set to 95 gAPI to highlight changes in bulk lithology.

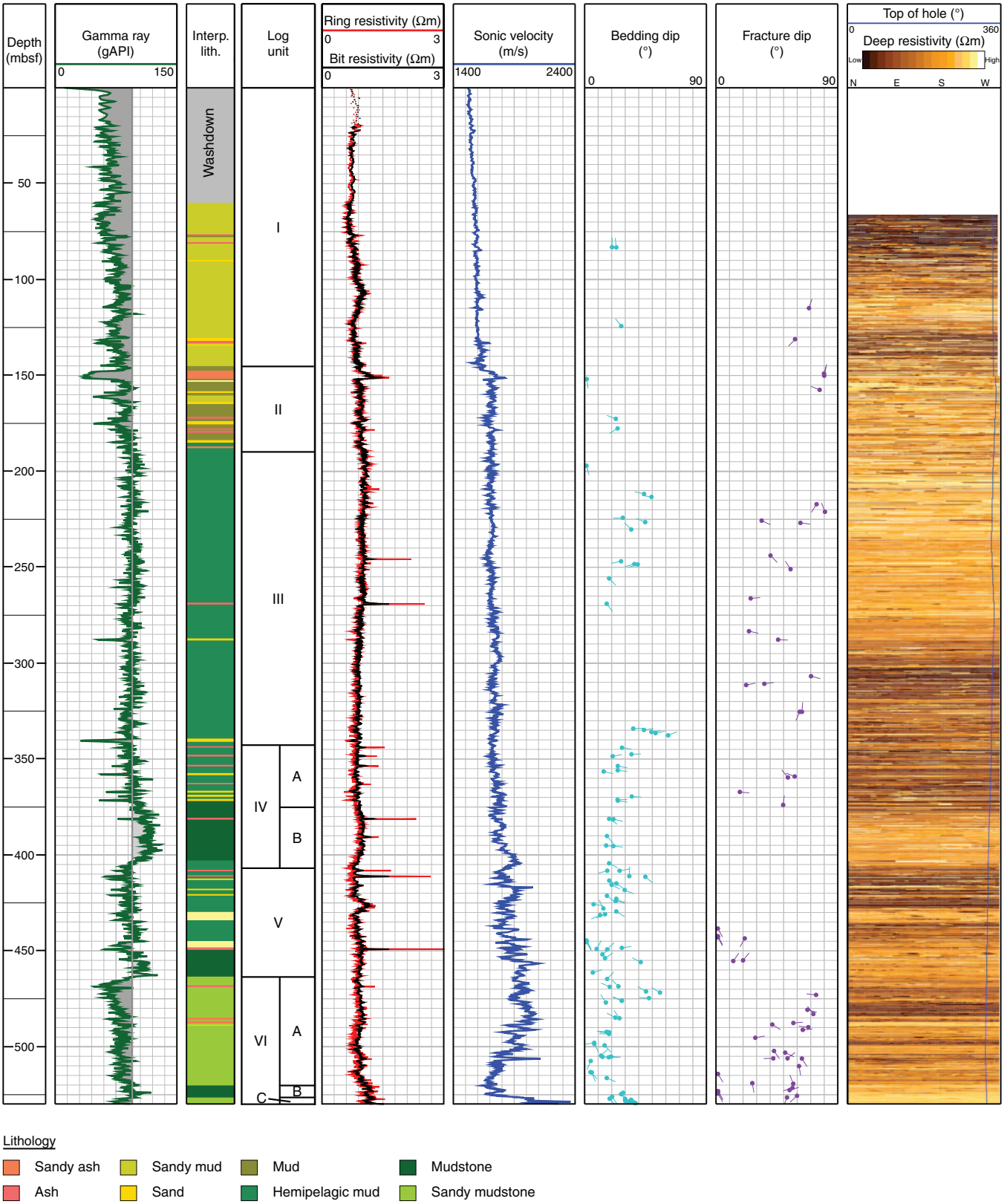

Figure F7. Composite plot of the LWD data for the basement section (530.3–710.0 mbsf), showing gamma ray, logging units, resistivity, sonic velocity, fracture dip, and deep button resistivity image. The gamma ray baseline was set to 18 gAPI, and gray shading highlights higher gamma ray values.

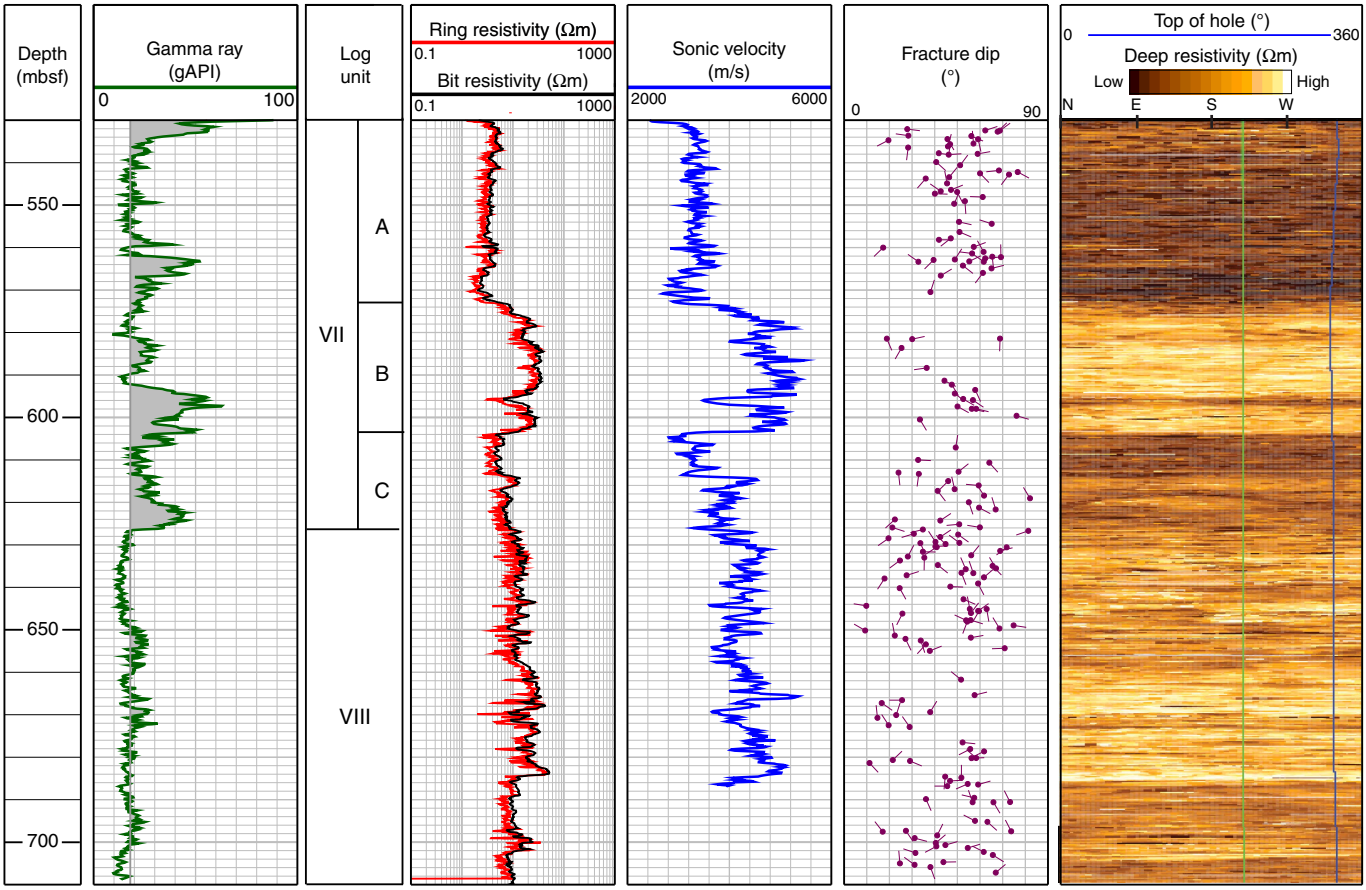

Figure F8. Plot of laboratory measured resistivity (R_{eff}) against MAD-derived porosity from Expedition 333 for the upper 180 m of Site C0012. Red line = Archie's law fit with parameters a = 1, m = 2.95, and coefficient of determination (R^2) = 0.78.

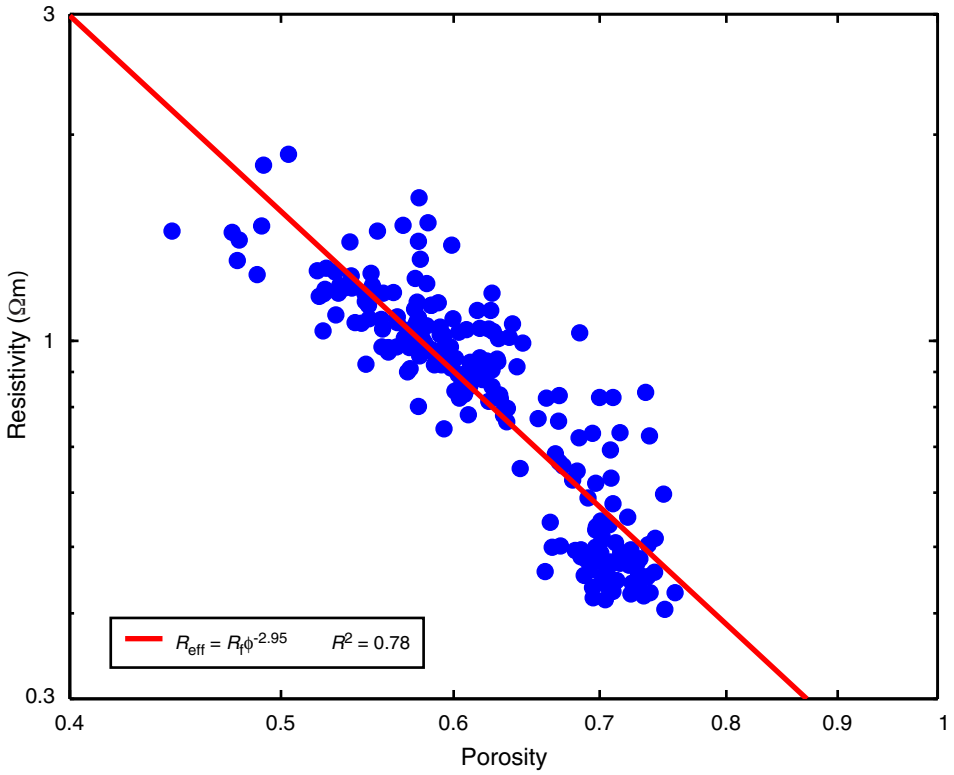

Figure F9. A. Resistivity-derived porosity (black line) plotted with moisture and density (MAD)-derived porosity from Expeditions 322 (blue = mudstone, yellow = sand) and 333 (red). Green lines show 1 standard deviation from the mean value of the resistivity-derived porosity trend. **B.** Offset $\Delta\phi = \phi_{MAD} - \phi_{resistivity}$ between the MAD-derived and resistivity-derived porosity trends. **C.** Resistivity-derived bulk density from porosity values in A.

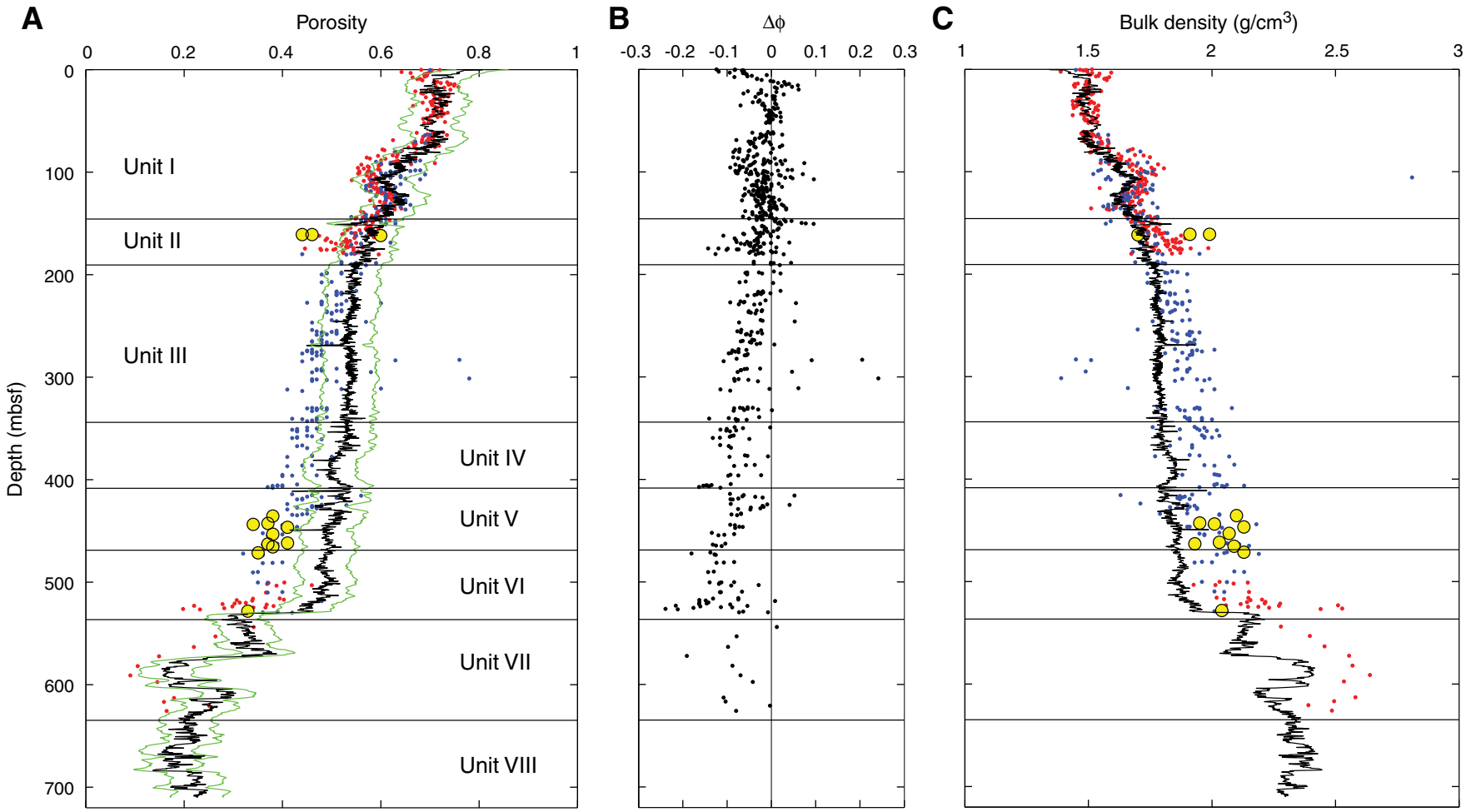

Figure F10. Textures and fractures observed in the basement, Hole C0012H. **A.** The irregular surface (i.e., nonplanar) at the sediment/basement interface (530.3 mbsf). **B.** Logging Subunit VIIA contains frequent variations in textural patterns (every 5 m or less), showing interpreted pillow basalt and thin sheet flow with subvertical fractures. **C.** Large, high-angle (~75°) low-resistivity (<7 Ωm) fracture bisecting a homogeneous sheet flow in logging Subunit VIIB. **D.** All three basement textures (mottled, turtleshell, and homogeneous zones) in logging Subunit VIIC. **E.** A sharp drop in resistivity marking the transition from a homogeneous zone to turtleshell texture at ~684 mbsf in logging Unit VIII, interpreted as the basal surface of a sheet flow. Several other (less distinct) surfaces are observed throughout both basement units. A and B are plotted on the medium range (0–10 Ωm) and C–E are plotted on the high range (2–50 Ωm) resistivity scale for static deep button resistivity.

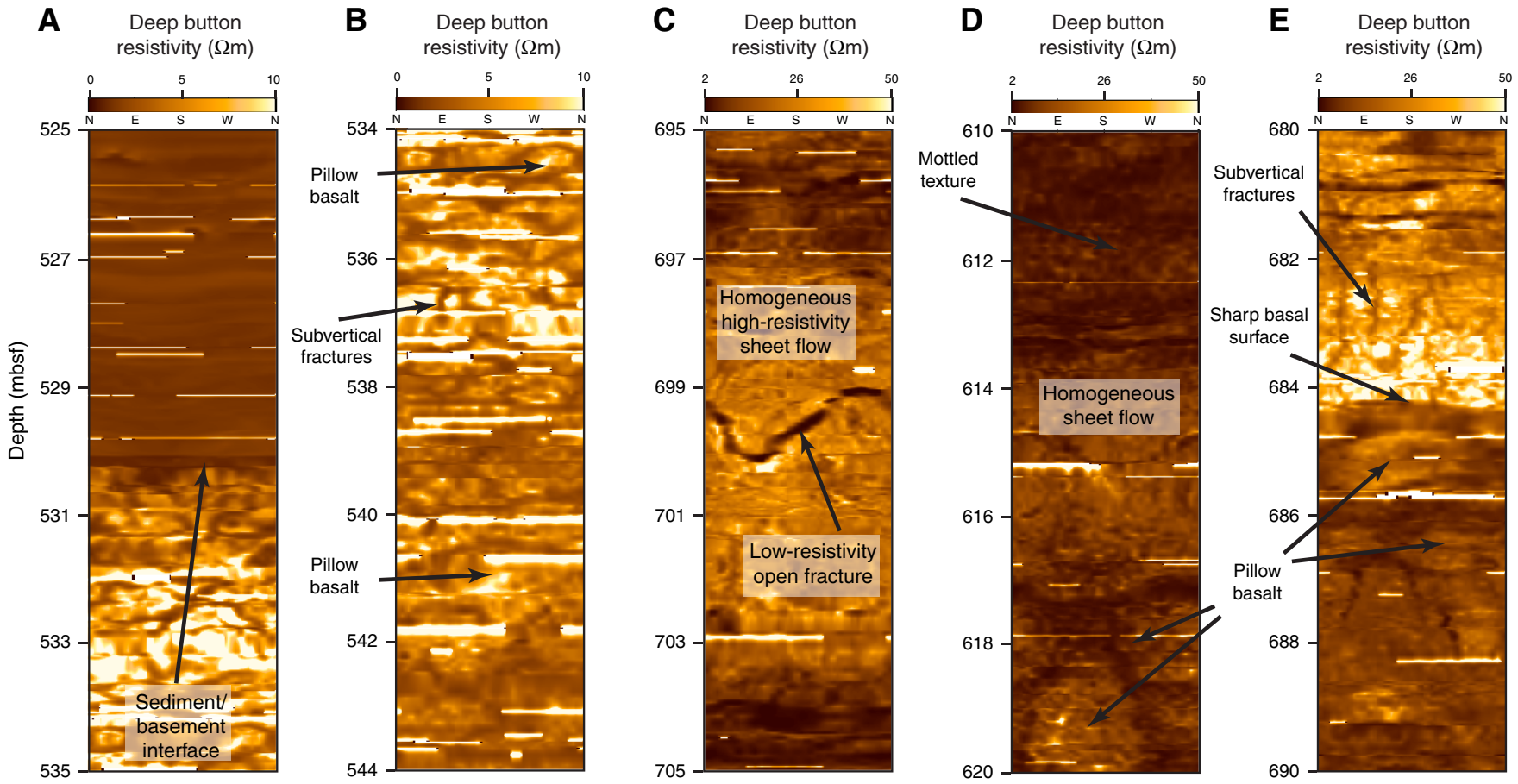

Figure F11. Stress-related structures observed in resistivity images. **A.** Breakouts in Shikoku Basin sediment. Low-range resistivity scale (0.5–1.5 Ωm) for static shallow button resistivity. **B.** Drilling-induced tensile fractures (DITFs) in the basement. High-range resistivity scale (2–50 Ωm) for static shallow button resistivity.

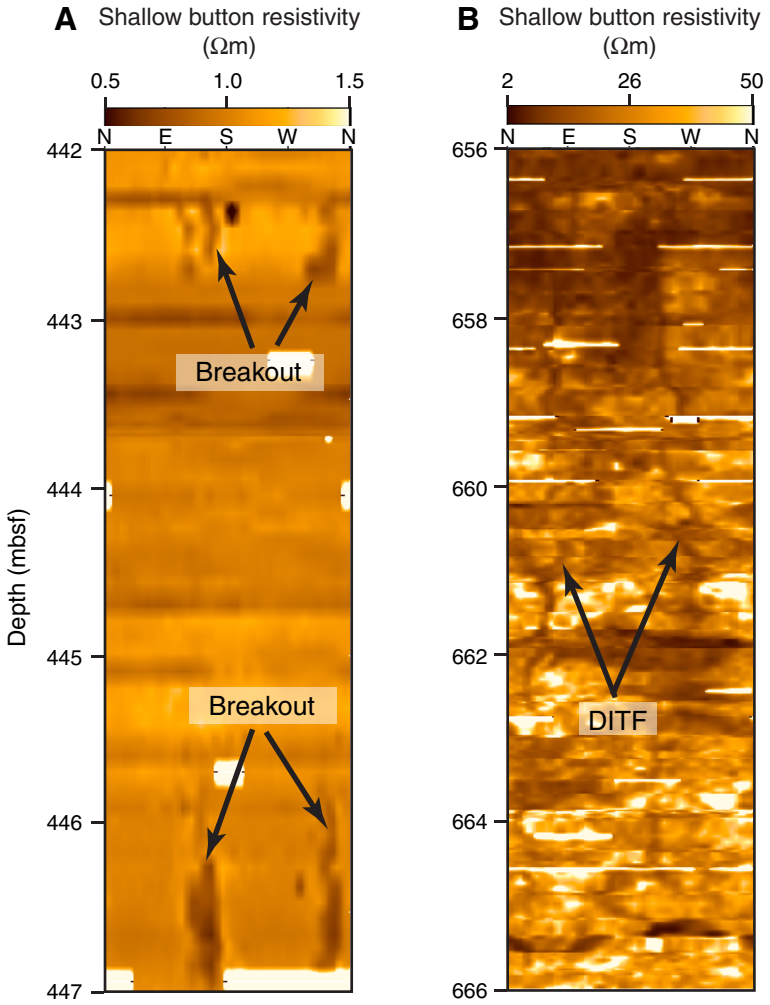

Figure F12. Core-log-seismic integration, Site C0012. LWD data from Hole C0012H with unit boundaries; core lithology from Holes C0012C, C0012D, and C0012A; and seismic data from In-line 95 of the IFREE 3-D PSDM volume (Park et al., 2008) showing the interpretation of Expedition 322 Scientists (2010c). Black dashed lines show correlations (? = tentative) between the unit boundaries identified for each data set. VE = vertical exaggeration.

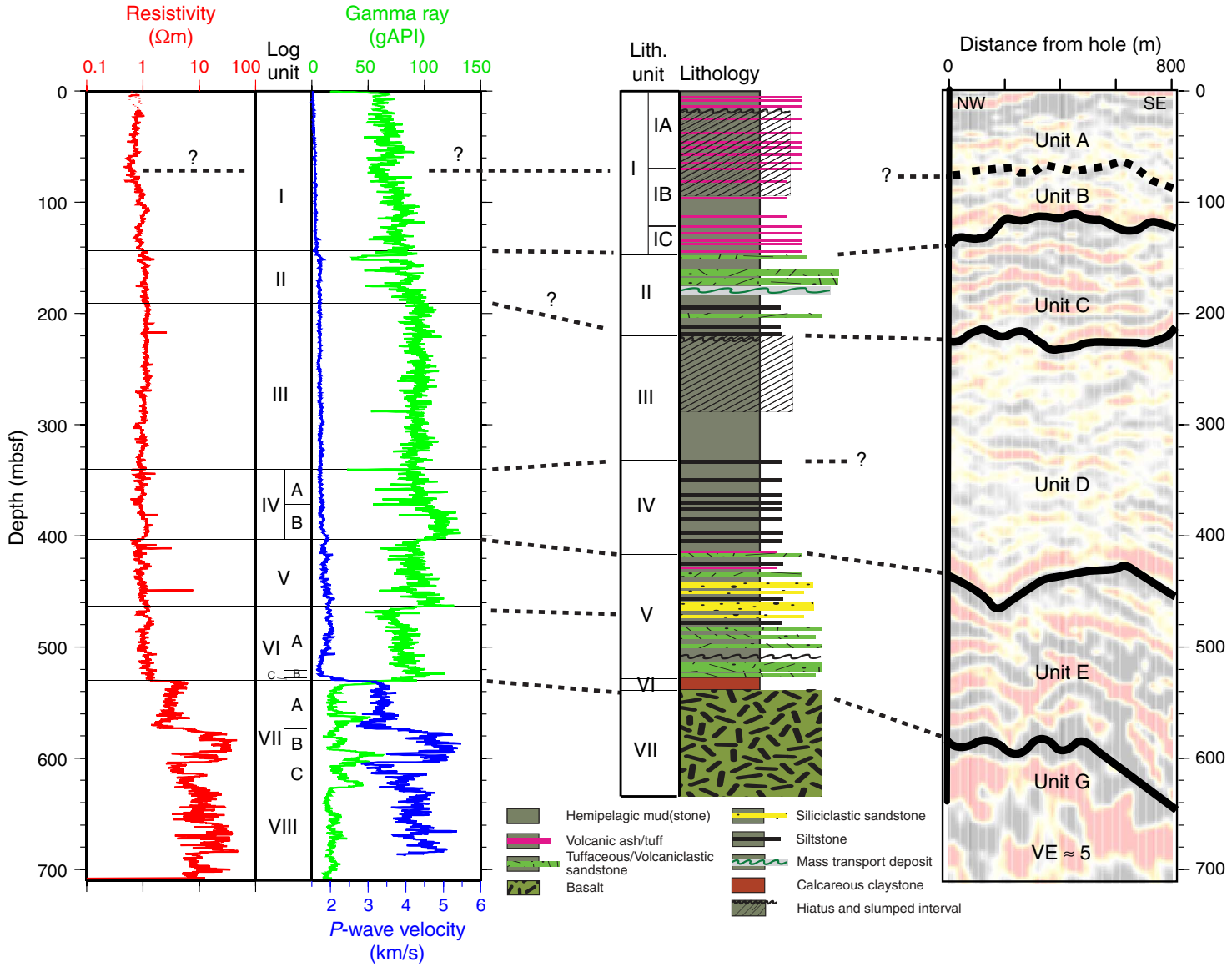

Table T1. Summary of LWD/MWD data and drilling parameters acquired in Hole C0012H.

Data	Raw	Processed	Processed by	Depth reference	Logs included	Data included	Available formats
Real time	x			Raw: DRF	Main	Gamma ray; shallow, medium, and deep button resistivity; compressional slowness; rate of penetration; downhole annular pressure; downhole annular temperature; downhole weight on bit; downhole torque; surface weight on bit; equivalent circulating density	DLIS, LAS, PDF
Memory data	x	x	LSS	Raw: DRF Processed: LSF (mbsf)	Main	Gamma ray; bit resistivity; ring resistivity; shallow, medium, and deep button resistivity; rate of penetration; rotational speed; collar rotational speed; downhole annular pressure; downhole annular temperature; downhole weight on bit; downhole torque; surface weight on bit; equivalent circulating density; equivalent static density; minimum and maximum static density; standpipe pressure; stick ratio	DLIS, LAS, PDF
Time	x	x	LSS	Time	Main	Borehole and bit depth; gamma ray; rate of penetration; rotational speed; collar rotational speed; downhole annular pressure; downhole annular temperature; downhole weight on bit; downhole torque; surface weight on bit; surface torque; equivalent circulating density; equivalent static density; minimum and maximum static density; standpipe pressure; stick ratio; axial, tool, and radial show level; Pump 1, 2, and 3 stroke rates; total stroke rate for all pumps; total flow rate of all active pumps; average hook load; status of the slips (in or out); status of the drill bit (on bottom); composite on bottom status	DLIS, LAS
Image logs		x	LSS	LSF (mbsf)	Main	Shallow, medium, and deep resistivity image logs with static normalization	DLIS, LAS, PDF
Sonic		x	SLB onshore	LSF (mbsf)	Main	Compressional slowness, compressional velocity	DLIS, LAS, PDF, SEGY
IMS data	x	x	LSS	Time: every 10 s interval Depth: DRF and LSF (mbsf)		Total depth, bit depth, rate of penetration, hook position, compensator position, hook load, weight on bit, power swivel torque, power swivel speed, standpipe manifold A pressure, standpipe manifold B pressure, mud Pump 1, mud Pump 2, mud Pump 3, mud Pump 4, active SPM, flow-in, mud return flow, total volume, gain/loss	CSV, TEXT

IMS = Information Management System on the *Chikyu*. LSS = logging staff scientist, SLB = Schlumberger. SPM = strokes per minute. DLIS = digital log information standard, LAS = log ASCII standard, SEGY = Society of Exploration Geophysicists format "Y", CSV = comma separated value.

Table T2. Defined logging unit boundary depths with the inferred dominant lithology, Hole C0012H.

Log unit	Depth (mbsf)	Subunit	Depth (mbsf)	Lithology
I	0–144.3			Sandy mud
II	144.3–188.1			Sandy mud with interbedded sands and ash
III	188.1–339.6			Hemipelagic mud
IV	339.6–403.3	A	339.6–372.1	Hemipelagic mud with sandy and ash layers
		B	372.1–403.3	Mudstone
V	403.3–463.5			Hemipelagic mud with sandy and ash layers
VI	463.5–530.3	A	463.5–520.4	Sandy mudstone
		B	520.4–526.7	Mudstone
		C	526.7–530.3	Sandy mudstone with high velocity
VII	530.3–626.6	A	530.3–572.9	Basement - basalt
		B	572.9–604.1	High resistivity/velocity basement
		C	604.1–626.6	Basement - basalt
VIII	626.6–710			Basement - basalt

Table T3. Summary of the textures observed in the basement, sorted by depth range, with resistivity ranges and preliminary interpretations, Hole C0012H.

Depth range (mbsf)	Thickness (m)	Deep resistivity (Ωm)	Texture	Preliminary interpretation
530.30–531.80	1.50	2–4	Turtleshell	Pillow basalt
531.80–534.30	2.50	3–10	Subvertical fractures	Sheet flow with cooling joints
534.30–535.75	1.45	2–4	Turtleshell	Pillow basalt
535.75–537.50	1.75	3–7	Subvertical fractures	Sheet flow with cooling joints
537.50–554.70	17.70	2–5	Turtleshell	Pillow basalt
554.70–557.00	2.30	2–4	Mottled	Volcaniclastics?
557.00–566.60	9.60	2–7	Turtleshell	Pillow basalt
566.60–570.50	3.90	0–2	Homogeneous	Sediments?
570.50–571.80	1.30	2–4	Subvertical fractures	Sheet flow with cooling joints
571.80–572.70	0.90	0–3	NA	Breakout?
572.70–576.50	3.80	3–12	Mottled	Volcaniclastics?
576.50–595.50	19.00	8–37	Subvertical fractures	Sheet flow with cooling joints
595.50–596.80	1.30	3–8	Turtleshell?	Pillow basalt
596.80–604.00	7.20	8–26	Subvertical fractures	Sheet flow with cooling joints
604.00–613.25	9.25	2–7	Mottled and turtleshell	Volcaniclastics?, pillows
613.25–617.25	4.00	4–13	Homogeneous	Solid sheet flow, DITF?
617.25–642.75	25.50	5–24	Turtleshell and mottled	Pillows, volcaniclastics?
642.75–644.30	1.55	4–28	Homogeneous	Solid sheet flow
644.30–650.10	5.80	7–18	Turtleshell	Pillow basalt
650.10–651.25	1.15	12–29	Homogeneous	Solid sheet flow
651.25–656.20	4.95	5–22	Turtleshell	Pillow basalt
656.20–678.00	21.80	5–32	Subvertical fractures	Sheet flow with cooling joints, DITF?
678.00–684.25	6.25	8–45	Subvertical fractures	Sheet flow with cooling joints
684.25–686.80	2.55	6–17	Turtleshell	Pillow basalt
686.80–689.25	2.45	6–13	Mottled and turtleshell	Volcaniclastics?, pillows
689.25–694.70	5.45	6–10	Mottled	Volcaniclastics?
694.70–697.50	2.80	6–15	Turtleshell	Pillow basalt
697.50–700.25	2.75	8–37	Subvertical fractures	Sheet flow with cooling joints, DITF?
700.25–701.40	1.15	8–17	Turtleshell	Pillow basalt
701.40–703.00	1.60	10–35	Homogeneous	Solid sheet flow
703.00–704.70	1.70	4–8	Mottled	Volcaniclastics?
704.70–708.40	3.70	5–10	Turtleshell	Pillow basalt

DITF = drilling-induced tensile fracture. NA = not applicable.

Table T4. Correlation of lithologic, logging, and seismic units, Hole C0012A.

Lithologic unit	Depth (mbsf)	Seismic unit (IFREE 3-D)	Depth (mbsf)	Log unit (C0012H)	Depth (mbsf)
I	0–150	A and B	0–120	I	0–166
II	150–215	C	120–200	II	166–188
III and IV	215–415	D	200–405	III and IV	188–403
V and VI	415–537	E	405–530	V and VI	403–530
VII	>537	G	>530	VII	>530

IFREE = Institute for Research on Earth Evolution.